

## A numerical solution to fluid-structure interaction of membrane structures under wind action

Fang-jin Sun<sup>1,2</sup> and Ming Gu<sup>\*2</sup>

<sup>1</sup>College of Civil Engineering and Architecture, Liaoning Technical University, Fuxin, Liaoning, 123000, China

<sup>2</sup>State Key Laboratory of Disaster Reduction in Civil Engineering, Tongji University, Shanghai 200092, China

(Received November 4, 2013, Revised March 17, 2014, Accepted April 1, 2014)

**Abstract.** A numerical simultaneous solution involving a linear elastic model was applied to study the fluid-structure interaction (FSI) of membrane structures under wind actions, i.e., formulating the fluid-structure system with a single equation system and solving it simultaneously. The linear elastic model was applied to managing the data transfer at the fluid and structure interface. The monolithic equation of the FSI system was formulated by means of variational forms of equations for the fluid, structure and linear elastic model, and was solved by the Newton-Raphson method. Computation procedures of the proposed simultaneous solution are presented. It was applied to computation of flow around an elastic cylinder and a typical FSI problem to verify the validity and accuracy of the method. Then fluid-structure interaction analyses of a saddle membrane structure under wind actions for three typical cases were performed with the method. Wind pressure, wind-induced responses, displacement power spectra, aerodynamic damping and added mass of the membrane structure were computed and analyzed.

**Keywords:** membrane structures; vibration under wind actions; fluid-structure interaction; numerical simultaneous solution

---

### 1. Introduction

Due to the high sensitivity to wind action and high geometric nonlinearity (undergoing large displacement), a key issue in wind resisting design of membrane structures is the interaction between wind and membrane structures (Li *et al.* 2012), i.e., fluid-structure interaction (FSI). Numerical simulation for studying FSI is becoming active with the rapid progress in hardware and software of computers.

To compute the FSI of membrane structures with numerical simulation, the following aspects are key issues: (a) choosing a proper method for coupling the fluid solver and the structural solver; (b) transferring the data between the fluid domain and the structural domain. For issue (a), the current solution strategies for FSI include partitioned solutions with loose coupling, partitioned solutions with strong coupling and simultaneous solutions. In loose-coupling schemes, separate solvers for fluid and structure are employed once per time step, resulting in a time lag between both continua. Strongly-coupled partitioned solutions require an additional iteration loop based on

---

\*Corresponding author, Professor, E-mail: [minggu@tongji.edu.cn](mailto:minggu@tongji.edu.cn)

the partial solvers, which demonstrate better convergence and stability characteristics, but additional numerical efforts are needed. The widely used loose-coupling method based on the simplified coupling procedure (Degroote *et al.* 2009) is appropriate for weak interactions between fluid and structure, since it may diverge in the case of strong interactions. Simultaneous procedures solve the coupled system in a single iteration loop with consistent time integration schemes for all physical fields, resulting in time-accurate coupled solutions. In other words, an anthology of numerical simultaneous solution is applied to FSI of membrane structures under wind actions, including formulating the fluid-structure system in a single equation system, and solving it simultaneously (Degroote *et al.* 2009). The merit of simultaneous procedures lies in its high accuracy and good convergence. The shortcomings are the large computational efforts, which can be overcome due to the rapid development of computers. For issue (b), a reasonable treatment of the fluid deformation plays a key role. The methods fall into two categories. Re-meshing the whole fluid domain is a traditional method, requiring excessive computational efforts. Due to the complex shape of membrane structures, the number and frequency of re-meshing should be diminished or avoided. Mesh moving is a relatively new yet more commonly-used method. The linear elastic model is the most commonly used model, an effective way to deal with large deformation (Stein *et al.* 2003), which considers node motion is governed by elastic equations, and the control of deformation is based on element size, shape and volume variation. Revuz *et al.* (2012) challenged the usual domain size guidance by studying the effects of changing the domain size around a tall building by CFD, employing RNG k-s turbulence model with the domain size as the only varied parameter, and the mesh resolution in the building/wake region as unchanged.

Most of the current studies on FSI of membrane structures, with numerical simulation, adopt partitioned solutions with loose-coupling or strong-coupling methods. Study on simultaneous solution method has been rather limited. A partitioned coupling algorithm, connecting a three-dimensional, finite volume based multi-block flow solver for incompressible fluids with a finite element code was applied to thin shells and membrane structures with large displacements (Glück *et al.* 2003). Wüchner *et al.* (2007) proposed a partitioned framework for analysis of thin membrane–wind interaction with the CFD software package CFX-5 and structure in-house finite element program CARAT. Michalski (2009) realized FSI simulation for lightweight structure based on partitioned approach with generation of wind flow by a three-dimensional fast Fourier transformation (FFT) technique in wave number space, where the turbulence is based on spectral tensors. Intensive fluid–structure interaction calculation was realized on a flexible 29 m umbrella membrane structure by Michalski *et al.* (2011) by coupling of CFD and CSD codes via a partitioned approach in an explicit manner. Habchi *et al.* (2013) developed the fluid-structure interaction solver in a partitioned approach using block Gauss-Seidel implicit scheme. Li *et al.* (2010) explored a useful approach for estimations of wind effects on complex curved roof by CFD techniques, where Large Eddy Simulation (LES) and Reynolds -averaged Navier-Stokes Equations (RANS) Model were employed. It was found that the recommended LES and inflow turbulence generation technique are useful to assess wind effects on a long-span roof.

As for simultaneous solution for FSI simulation, the space–time finite element method is applied to both fluid and structure continua, leading to formulating fluid, structure and coupling conditions in a single equation system (Hübner *et al.* 2004.). The method was applied to a 2D membrane example, and the results described the interaction of separated vortex and the membrane. Though a simultaneous solution procedure for FSI study has had limited use, studies have shown its superiority in stability and accuracy in computation (Habchi *et al.* 2013, Richter *et al.* 2013). Thus, for strong interactions such as the case of wind and membrane structures,

simultaneous solution procedures may be preferable in order to ensure stability and to accelerate convergence of the coupled solution.

The work here employs the simultaneous procedures to study the fluid-structure interaction of membrane structures under wind actions to obtain more accurate solutions and illustrate the FSI mechanism of membrane structures. A linear elastic model was applied to manage the fluid deformation. The monolithic coupling was achieved through implicit treatment of equilibrium conditions at the interface. The strongly monolithic equations of the FSI system were derived through the variational forms of equations for fluid, structure and the linear elastic model. The monolithic equations were solved by Newton-Raphson method for simultaneous solutions, with the programming and implementation procedures illustrated. The uniqueness of the study here is the application of linear elastic model in the monolithic equations to obtain the simultaneous solutions for the FSI of membrane structures under wind actions.

## 2. Governing equations and boundary conditions

### 2.1 Fluid dynamics

The incompressible viscous fluid is governed by the Navier–Stokes equations, consisting of momentum conservation and continuity equation

$$\nabla \cdot \mathbf{v}_f = 0 \quad (1)$$

$$\rho_f \left( \frac{\partial \mathbf{v}_f}{\partial t} + \mathbf{v}_f \cdot \nabla \mathbf{v}_f \right) = \nabla \cdot \boldsymbol{\sigma}_f + \mathbf{f}_f^B \quad (2)$$

where  $\boldsymbol{\sigma}_f$  is total stress tensor (pressure and viscous stress),  $\boldsymbol{\sigma}_f = \mu[\nabla \mathbf{v}_f + (\nabla \mathbf{v}_f)^T] - p\mathbf{I}$ ,  $\mu$  is the fluid viscosity,  $\mathbf{v}_f$  is the fluid velocity,  $p$  is the fluid pressure,  $\mathbf{f}_f^B$  is the fluid unit body force.  $\rho_f$  is the fluid density,  $\nabla$  represents spatial gradient.

The boundary conditions of the fluid are defined as

$$\mathbf{v}_f = \bar{\mathbf{v}}_f, \text{ on } \Gamma_D^f \quad (3)$$

$$\boldsymbol{\sigma}_f \cdot \mathbf{n}_f = \bar{\mathbf{f}} \text{ on } \Gamma_N^f \quad (4)$$

$$\mathbf{v}_f = \dot{\mathbf{u}}_s^{FSI} \text{ on } \Gamma_I \quad (5)$$

where  $\Gamma_D$ ,  $\Gamma_N$  and  $\Gamma_I$  represent the fluid Dirichlet boundary, Neumann boundary and interface between fluid and solid, respectively,  $\bar{\mathbf{v}}_f$  is specified velocity on the Dirichlet boundary,  $\dot{\mathbf{u}}_s^I$  is the fluid velocity at the interface  $\Gamma_I$ ,  $\bar{\mathbf{f}}$  is specified traction on  $\Gamma_N$ ,  $\mathbf{n}_f$  is the outward unit vector normal to the fluid boundary.

## 2.2 Structural dynamics

The governing equations for the structure are described by a total Lagrangian (T.L.) formulation and a large deformation theory. Considering material nonlinearity of membrane structures, the constitutive relationship of the structure can be described by the hyperelastic St.Venant-Kirchoff model (Gil 2006). For details, it can be referred to in Gil (2006).

In the T.L. formulation, differential equilibrium equations based on initial un-deformed configuration can be expressed as

$$\nabla \cdot \boldsymbol{\sigma}_l + \mathbf{f}_s = 0 \quad (6)$$

where  $\boldsymbol{\sigma}_l$  stands for Piola-Lagrange stress tensor, the deformed stress in terms of un-deformed configuration,  $\boldsymbol{\sigma}_l = \mathbf{F}\boldsymbol{\sigma}_p$  and  $\mathbf{F} = \mathbf{I} + \mathbf{h}$ ,  $\mathbf{f}_s$  is a body force.

The Green-Lagrange strain tensor is defined as

$$\mathbf{E} = \frac{1}{2}(\mathbf{h} + \mathbf{h}^T + \mathbf{h}^T\mathbf{h}) \quad (7)$$

where  $\mathbf{h} = \nabla x$  represents displacement gradient tensor on the un-deformed or initial configuration ( $x = \xi\mathbf{e}_x + \eta\mathbf{e}_y$  is displacement).

The boundary conditions are written as

$$\mathbf{u}_s = \bar{\mathbf{u}}_s \quad \text{on } \Gamma_N^s \quad (8)$$

$$\boldsymbol{\sigma}_l \cdot \mathbf{n}_s = \bar{\mathbf{t}}_s \quad \text{on } \Gamma_D^s \quad (9)$$

where  $\mathbf{u}_s$  is the unknown structural displacement,  $\bar{\mathbf{u}}_s$  represents prescribed surface on the prescribed Neumann boundary,  $\bar{\mathbf{t}}_s$  stands for prescribed displacement on Dirichlet boundary,  $\mathbf{n}_s$  denotes the outward unit vector normal to the solid boundary.

## 2.3 Fluid-structure interaction

One of the priorities in fluid-structure interaction is to deal with the data transfers at the interface between the fluid and solid, involving the displacement and traction. In the present study, a linear elastic model is applied to manage the fluid deformation at the interface, enforcing momentum conservation and geometric continuity at the interface. The linear elastic model can be expressed as (Stein *et al.* 2003)

$$\nabla \cdot \boldsymbol{\sigma}_l^{LE} = 0, \quad (10)$$

$$\mathbf{E}^{LE} = \frac{1}{2}[\mathbf{h}^{LE} + (\mathbf{h}^{LE})^T]. \quad (11)$$

$$\boldsymbol{\sigma}_{p(ij)}^{(LE)} = \boldsymbol{\sigma}_{c(ij)}^{LE} + \mathcal{G}_{(ijkl)}^{LE} \mathbf{E}_{kl}^{(LE)} \quad (12)$$

where  $\boldsymbol{\sigma}_l^{LE}$  denotes Piola-Lagrange stress tensor of the linear elastic model,  $\mathbf{E}^{LE}$  is

Green-Lagrange strain tensor of the linear elastic model,  $\boldsymbol{\sigma}_p^{LE}$  represents Piola-Kirchoff stress tensor of the linear elastic model.

The boundary conditions of the above equations are expressed as

$$\mathbf{u}_{LE}^{FSI} = 0 \quad \text{on } \Gamma_{FSI} \quad (13)$$

where  $\mathbf{u}_{LE}^{FSI}$  denotes the linear elastic model displacement at the interface,  $\Gamma_{FSI}$  represents the solid and the fluid interface, that is, the linear elastic model displacement at the interface equals zero.

The coupling conditions at the interface are written as:

$$\mathbf{u}_{LE}^{FSI} = \mathbf{u}_s^{FSI}, \text{ on } \Gamma_{FSI} \quad (14)$$

$$\mathbf{v}_f^{FSI} = \mathbf{v}_s^{FSI}, \text{ on } \Gamma_{FSI} \quad (15)$$

$$\boldsymbol{\sigma}_c^{FSI} \cdot \mathbf{n}_s + \boldsymbol{\sigma}_f^{FSI} \cdot \mathbf{n}_f = 0 \text{ on } \Gamma_{FSI} \quad (16)$$

where  $\mathbf{v}_s$  represents the structural velocity,  $\boldsymbol{\sigma}_c$  denotes Cauchy stress,  $\boldsymbol{\sigma}_c = \mathbf{F}\boldsymbol{\sigma}_p\mathbf{F}^T / J$ ,  $J = \det(\mathbf{F})$  stands for jacobian,  $\mathbf{n}_s = -\mathbf{n}_f$ .

#### 2.4 Monolithic equations for fluid-structure interaction

In order to weaken the requirements of continuity for the solution, variation forms of equations for the fluid, structure and the linear elastic model are employed to compose the monolithic equations. Before deriving the monolithic equations, discretization for the fluid, structure and linear elastic model are required. The fluid, structural and linear elastic equations, i.e., Eq. (1), Eq. (2), Eq. (6) and Eq. (10), are discretized by Galerkin finite element method, and implicit finite difference method is employed for time discretization. The discretization is the process for deriving the weak forms of the equations through weighted residual method.

The weighted residual form of the momentum Eq. (1) is expressed as

$$\int_{\Omega^f} \omega \nabla \cdot \mathbf{v}_f d\Omega = 0 \quad (18)$$

The weighted residual form of the continuous Eq. (2) can be written as

$$\int_{\Omega^f} \left( -\zeta \cdot \rho_f \left( \frac{\partial \mathbf{v}_f}{\partial t} + \mathbf{v}_f \cdot \nabla \mathbf{v}_f \right) - \nabla \zeta : \boldsymbol{\sigma} + \zeta \cdot \mathbf{f}_f \right) d\Omega + \int_{\Gamma_N^f \cup \Gamma_{FSI}} \zeta \cdot (\boldsymbol{\sigma}_f \cdot \mathbf{n}_1^f) d\Gamma = 0 \quad (19)$$

where  $\Omega$  stands for spatial domain composed of  $\Gamma_D$ ,  $\Gamma_N$  and  $\Gamma_{FSI}$ ,  $\Omega_f$  represents fluid domain,  $\Gamma_N$  and  $\Gamma_{FSI}$  represents Neumann boundary and the fluid-structure interface, respectively,  $\omega$  and  $\zeta$  denote test functions.

The weighted residual form of the structural Eq. (6) reads

$$-\int_{\Omega_0^s} (\nabla \eta : \boldsymbol{\sigma}_l - \eta \cdot \mathbf{f}_s) d\Omega + \int_{\Gamma_{N0}^s \cup \Gamma_{FSI0}} ((\eta \cdot \mathbf{n}_0^s) : \boldsymbol{\sigma}_l) d\Gamma = 0 \quad (20)$$

where  $\eta$  is a test function,  $\Omega_0^s$  and  $\Gamma_{FSI0}$  represent initial configuration of structure domain and initial configuration at the interface, respectively.

The weighted residual form of the linear elastic Eq. (10) reads

$$-\int_{\Omega_0^s} (\nabla \eta : \boldsymbol{\sigma}_l^{LE}) d\Omega + \int_{\Gamma_{N0}^s} ((\eta \cdot \mathbf{n}_0^s) : \boldsymbol{\sigma}_l^{LE}) d\Gamma = 0 \quad (21)$$

The weighted residual form of the coupling conditions (16) is expressed as

$$\int_{\Gamma_{FSI0}} \eta \cdot \boldsymbol{\sigma}_l \cdot \mathbf{n}_s^0 d\Gamma + \int_{\Gamma_{FSI1}} \zeta \cdot \boldsymbol{\sigma}_f \cdot \mathbf{n}_f^1 d\Gamma = 0 \quad (22)$$

where the first term represents the structure contribution on the initial configuration, the second term stands for the fluid contribution on the deformed mesh.

Adopting one-step- $\theta$ -time discretization, the discretizing form of the coupling condition (15) can be written as

$$\mathbf{v}_f^{n+1} = \frac{1}{\theta} \frac{d\mathbf{d}_{FSI}^{u,n+1} - d\mathbf{d}_{FSI}^{u,n}}{dt} - \frac{1-\theta}{\theta} \mathbf{v}_f^n \quad (23)$$

where the parameter  $\theta$  satisfies  $1/2 \leq \theta \leq 1$ . (Förster *et al.* 2005)

Then Eq. (14) representing the relationship between the linear elastic model displacement and fluid velocity can be expressed as

$$\mathbf{u}^{LE,n+1} = \mathbf{u}^{LE,n} + \theta \Delta t \mathbf{v}_f^{n+1} + (1-\theta) \Delta t \mathbf{v}_f^n \quad (24)$$

To obtain the strongly coupled monolithic equations of the nonlinear system, combining Eq. (18) with Eq. (22), the weighted residual equations  $\mathbf{f}_{FSI}$  of the FSI reads

$$\mathbf{f}_F = \int_{\Omega^f} (\omega \nabla \cdot \mathbf{v}_f + \zeta \cdot \rho_f \left( \frac{\partial \mathbf{v}_f}{\partial t} + \mathbf{v}_f \cdot \nabla \mathbf{v}_f \right) - \nabla \zeta : \boldsymbol{\sigma}_f + \zeta \cdot \mathbf{f}_f) d\Omega = 0 \quad (25)$$

$$\mathbf{f}_S = \int_{\Omega_0^s} (\nabla \eta : \boldsymbol{\sigma}_l - \eta \cdot \mathbf{f}_s) d\Omega = 0 \quad (26)$$

$$\mathbf{f}_{LE} = \int_{\Omega_0^s} (\nabla \eta : \boldsymbol{\sigma}_l^{LE}) d\Omega = 0 \quad (27)$$

$$\mathbf{f}_F^{FSI} = \int_{\Gamma_N^f \cup \Gamma_{FSI}} \zeta \cdot (\boldsymbol{\sigma}_f \cdot \mathbf{n}_f^1) d\Gamma = 0 \quad (28)$$

$$\mathbf{f}_S^{FSI} = \int_{\Gamma_N^s \cup \Gamma_{FSI}} ((\eta \cdot \mathbf{n}_s^0) : \boldsymbol{\sigma}_l) d\Gamma = 0 \quad (29)$$

where  $\mathbf{f}_F$ ,  $\mathbf{f}_S$  and  $\mathbf{f}_{LE}$  denote weighted residual form of the fluid, solid and linear elastic model equations, respectively,  $\mathbf{f}_F^{FSI}$  and  $\mathbf{f}_S^{FSI}$  represent weighted residual form of the coupling conditions at the interface, the unknowns of the monolithic equations are the fluid velocity  $\mathbf{v}_f$ , pressure  $P$ ,

linear elastic model displacement  $\mathbf{u}^{ES}$  and structural displacement  $\mathbf{u}_s$ .

Finally, along the interface, linear elastic model displacements are implicitly imposed to be equal with structural displacements in a strong sense

$$\mathbf{u}^{ES} = \mathbf{u}_s \text{ (on } \Gamma_I \text{)} \quad (30)$$

The monolithic equations of the fluid-structure are solved using Newton-Raphson method, posteriori error employed.

### 3. Solution approach

The above monolithic equations are composed of equations for the fluid ( $K_f$ ), the structure ( $K_s$ ), and the linear elastic model ( $K_u$ ), which need to be solved iteratively in a single time step. The fluid loads will be transferred to the structure as implicit unknown reactions. Here Newton-Raphson method is employed to solve the equations, which can be written as:

$$\frac{d\mathbf{f}_{FSI}}{dx} \Delta \mathbf{x}_i = -\mathbf{f}_{FSI}^i \quad (31)$$

where  $\mathbf{x}$  represents all the unknowns in the equations,  $\mathbf{J}^{FSI} = \frac{d\mathbf{f}_{FSI}}{dx}$  is Jacobian matrix,  $i$  stands for iterative time step.

In terms of the simultaneous solution in the present work, Eq. (31) can be further written as

$$\begin{bmatrix} \frac{\partial \mathbf{f}_s}{\partial \mathbf{u}_s} & \delta \frac{\partial \mathbf{f}_s}{\partial \mathbf{u}_s^{FSI}} \\ \frac{\partial \mathbf{f}_s^{FSI}}{\partial \mathbf{u}_s} & \delta \left( \frac{\partial \mathbf{f}_s^{FSI}}{\partial \mathbf{u}_s^{FSI}} + \frac{\partial \mathbf{f}_F^{FSI}}{\partial \mathbf{u}_s^{FSI}} \right) + \frac{\partial \mathbf{f}_F^{FSI}}{\partial \mathbf{v}_f} & \frac{\partial \mathbf{f}_F^{FSI}}{\partial \mathbf{u}_{LE}} & \frac{\partial \mathbf{f}_F^{FSI}}{\partial \mathbf{u}_{LE}} \\ & \delta \frac{\partial \mathbf{f}_F^{FSI}}{\partial \mathbf{u}_{LE}^{FSI}} + \frac{\partial \mathbf{f}_F^{FSI}}{\partial \mathbf{v}_f} & \frac{\partial \mathbf{f}_F^{FSI}}{\partial \mathbf{v}_f} & \frac{\partial \mathbf{f}_F^{FSI}}{\partial \mathbf{u}_{LE}} \\ & \delta \frac{\partial \mathbf{f}_{LE}^{FSI}}{\partial \mathbf{u}_{LE}^{FSI}} & & \frac{\partial \mathbf{f}_{LE}^{FSI}}{\partial \mathbf{u}_{LE}} \end{bmatrix} \begin{bmatrix} \Delta \mathbf{u}_s^i \\ \Delta \mathbf{v}_f^{FSI,i} \\ \Delta \mathbf{v}_f^i \\ \Delta \mathbf{u}_{LE}^i \end{bmatrix} = -\mathbf{f}_{FSI}^i \quad (32)$$

where  $\mathbf{v}_f$  represents for all the unknowns of the fluid domain, including fluid velocity and pressure,  $\delta = \theta \Delta t$ .

As for the displacement increment and velocity increment, the following relationship reads

$$\Delta \mathbf{u}_s^{FSI,i} = \delta \Delta \mathbf{v}_f^{FSI,i} \quad (33)$$

$$\mathbf{u}_s^{i+1} = \mathbf{u}_s^i + \Delta \mathbf{u}_s^i \quad (34)$$

$$\mathbf{v}_f^{i+1} = \mathbf{v}_f^i + \Delta \mathbf{v}_f^i \quad (35)$$

$$\mathbf{u}_{LE}^{i+1} = \mathbf{u}_{LE}^i + \Delta \mathbf{u}_{LE}^i \quad (36)$$

Eq. (32) will be updated and solved in each time step to obtain each unknown of the equations.

To avoid Eq. (31) being ill conditioned, a pre-conditioner based on the generalized minimal residual method (GMRES) (Heil 2004), with left preconditioning, is applied.

#### 4. Simultaneous solution procedures

FORTTRAN was adopted for programming the meshing and solution codes with parallel computing. Commercial software ANSYS is used to call the above FORTRAN programs as subroutines, where APDL is used for the secondary development. The computer configuration is: Intel i5 3450S, CPU frequency of 2800MHz, memory capacity of 4GB DDR3.

The simultaneous solution procedures are shown in Fig. 1, which can be divided into the following modules.

(1). Geometric model. Commercial software ANSYS is applied to establish the geometrical model of membrane structures, known as form-finding.

(2). Mesh the system. Meshing covers the fluid domain, structure domain and interface. The linear elastic model was applied to manage the deformation of the fluid domain to approximate the deformed fluid boundary. The interface was discretized on the basis of the mesh density, determined by the linear elastic model displacement. For the boundary conditions, the coupling of the fluid and structure is achieved through imposing motion and equilibrium conditions, including displacement and velocity (zero at the interface) (Etienne *et al.* 2004). Displacement of the linear elastic model is set to be equal to the structural displacement at the interface, and initial values are assigned to the internal nodal variable.

(3). Solve the monolithic equations. The Newton-Raphson method was chosen to produce the simultaneous solutions in each time step. The meshing results and solutions are saved as multi-dimensional dynamic arrays. The solution procedures for the monolithic equations are shown in Fig. 2, to be discussed in the following part. The inner loop was executed at least once, before going to the Newton-Raphson update.

(4). Error estimate. The theory of finite element states that stresses converge to their exact values as the mesh is refined. Hence, the quality of the solution can be measured by computing the norms of the computed element stress and the exact stress. The exact stresses can be replaced by a continuous approximation obtained by local least-squares projection (Zienkiewicz and Zhu 1992). When the solutions converge to the specified value, the following computation was started. The FSI loop was executed at least once before output the results.

(5). Output results. After cycling of all the time steps, the final results of displacements, pressure, velocity, etc. are saved and output. APDL language in commercial software ANSYS is applied to call the FORTRAN subroutines. The post processing of the results is completed by interfacing with ANSYS. Parameters such as wind pressure coefficients, responses of the structure under wind action are obtained.

Solution procedures of the unknowns  $\mathbf{v}_{ft}^i$ ,  $p_{ft}^i$ ,  $\mathbf{u}_t^i$  and  $\mathbf{u}_{st}^i$  for the monolithic equations at the  $i$ th iteration step of time step  $t$  are shown in Fig. 2. The details are introduced briefly below.

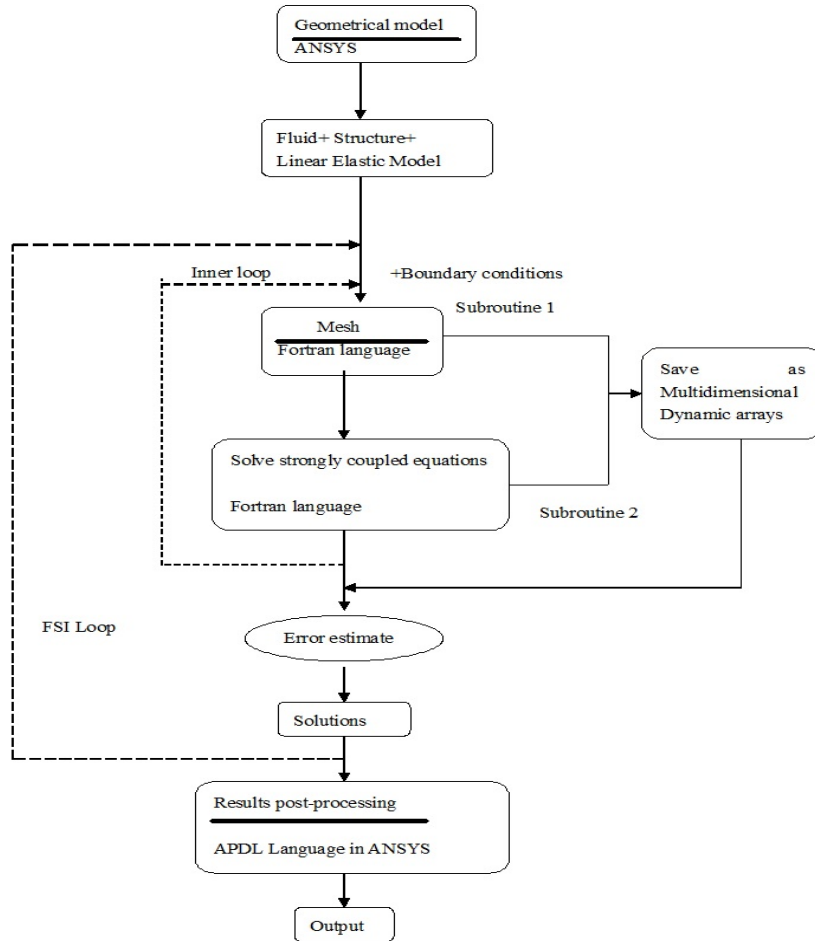


Fig. 1 Numerical simultaneous solution procedures

(1). Start iteration from a zero initial field for all variables in the equations to ensure convergence of Newton’s Method. Implicitly treat the boundary conditions and loads at the interface of the entire fluid-structure interaction system. All the fluid variables were saved on the mesh nodes.

(2). Newton-Raphson method was applied to get the simultaneous solutions of the monolithic equations. For linear equations  $\mathbf{A}(\mathbf{x}_t^{i-1}) \cdot \mathbf{x}_t^i = \mathbf{b}(\mathbf{x}_{t-1}^i, \mathbf{x}_t^{i-1})$ , the boundary conditions are introduced for iterative computation.

(3). With the help of the values of the previous iteration step,  $\mathbf{x}_t^{i-1}$  obtained from the (i-1) iteration step for time step t were considered as knowns to solve the linear equations,  $\mathbf{A}(\mathbf{x}_t^{i-1}) \cdot \mathbf{x}_t^i = \mathbf{b}(\mathbf{x}_{t-1}^i, \mathbf{x}_t^{i-1})$ . For the first time step, the solution obtained from the last iteration of

the previous time step was treated as the initial solution of the current time step.

(4). After obtaining the unknowns  $\mathbf{v}_{ft}^i, p_{ft}^i, \mathbf{u}_t^i$  and  $\mathbf{u}_{st}^i$  of the  $i$ th iteration step, update the mesh for the  $(i+1)$ th iteration step for the  $(i+1)$ th iteration. Meanwhile, enforce the linear elastic model displacement to be equal to the structural displacement at the interface, i.e.,  $\mathbf{u}_t^{i+1} = \mathbf{u}_{st}^i$  (on  $\Gamma_I$ ).

(5). Divide the fluid boundary according to the linear elastic model displacement  $\mathbf{u}_t^{i+1}$ . Interpolate the solution field from the  $i$ th iteration step mesh to the  $(i+1)$ th iteration step mesh to obtain the deformed fluid boundary. After getting the deformed boundary, mesh the fluid domain and structure domain.

(6). Update the mesh of the system. After obtaining the solutions of the monolithic equations, due to the distortion of the structural displacement, it is necessary to update the system mesh on the deformed configuration to avoid distortion of the fluid mesh and extreme distorted elements.

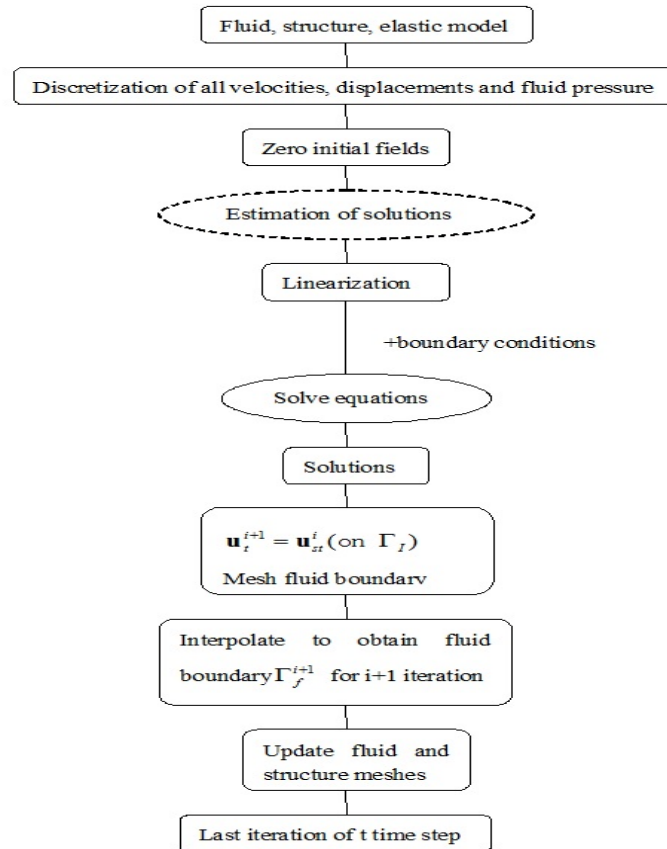


Fig. 2 Solutions to the monolithic equations

## 5. Validation of the numerical simultaneous solution

### 5.1 Flow around circular cylinders at different Reynolds number

To validate the accuracy of the monolithic solution procedures above, flow around a circular cylinder at low Reynolds number ( $Re=300$ ) was simulated first, since the accuracy of fluid computation is vital for the FSI calculation. The computation conditions are referred to in Lima *et al.* (2003). The pressure distribution at  $Re=300$  is shown in Fig. 3. Vortex shedding, and the phenomenon of the Karman vortex street, can be seen clearly in the figure.

Comparisons of mean drag coefficients at different Reynolds number using the present method and results from previous studies (Park *et al.* 1998, Ye *et al.* 1999) are shown in Table 1. The present results agree well with those from the previous studies.

To verify the effectiveness of the present method, computation of flow around cylinders at high Reynolds number was also performed, which is referred to the computation conditions in Catalano *et al.* (2003). The  $k-\omega$  based SST model is employed for turbulence simulation. The  $k-\omega$  based SST model and related parameters are the same as those used by Yang and Gu (2008, 2009). Fig. 4 shows the mean wind pressure distribution on the cylinder surface at  $Re=10^6$  ( $C_p = (p_c - p_\infty) / (0.5\rho U_\infty^2)$ , where  $p_c$  is static pressure at circumferential angle  $\theta$  of the cylinder,  $\theta$  is measured clockwise from the stagnation point,  $p_\infty$  is the fluid static pressure at infinite point.). Comparisons are made between the results computed here with those in Catalano *et al.* (2003) and Singh *et al.* (2005), where Catalano *et al.* (2003) adopted large eddy simulation (LES), and Singh *et al.* (2005) solved two dimensional N-S equations numerically by steady finite element equations. The maximum difference is about 8% with those in Singh *et al.*, and about 11% with those in Catalano *et al.* (2003).

Fig. 5 gives non-dimensional instantaneous vorticity magnitude ( $wD/U_\infty$ ) contours of flow around the cylinder at  $Re=10^6$ , from which vortex shedding can be obviously observed.

To validate stability of the present method, the case at  $Re=3.6 \times 10^6$  is also performed. Fig. 6 shows the predicted mean drag coefficients, which are compared with the ones in Catalano *et al.* (2003) and Singh *et al.* (2005). It can be seen that the results computed in this work compare well with those in the previous studies.

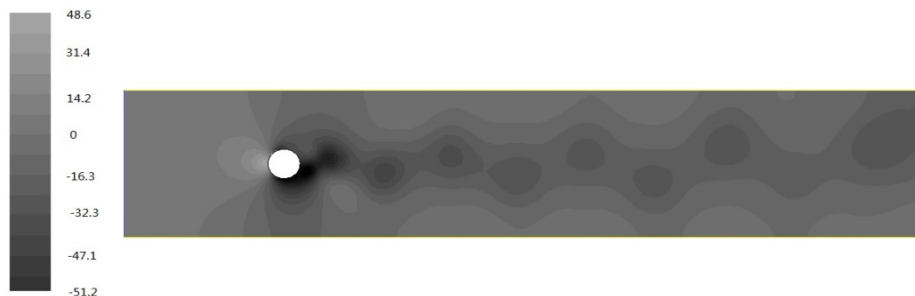


Fig. 3 Pressure distribution at  $Re=300$

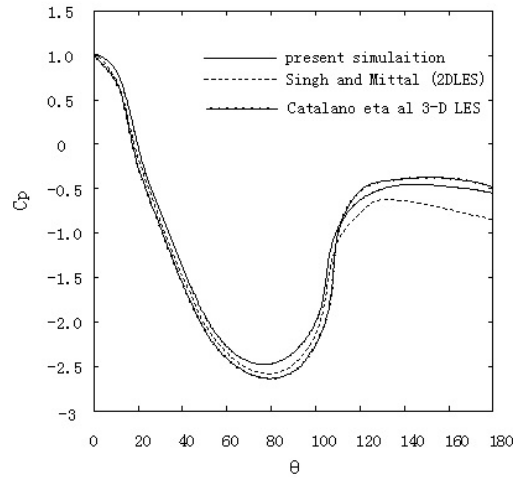


Fig. 4 Mean wind pressure distribution on the cylinder

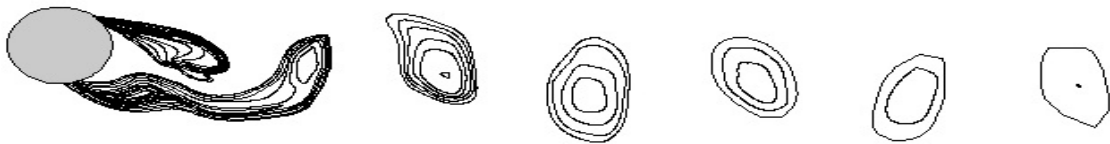


Fig. 5 Non-dimensional instantaneous vorticity magnitude contours of flow around the cylinder at  $Re=10^6$  from  $wD/ =1$  to  $wD/ =450$  (exponential distribution)

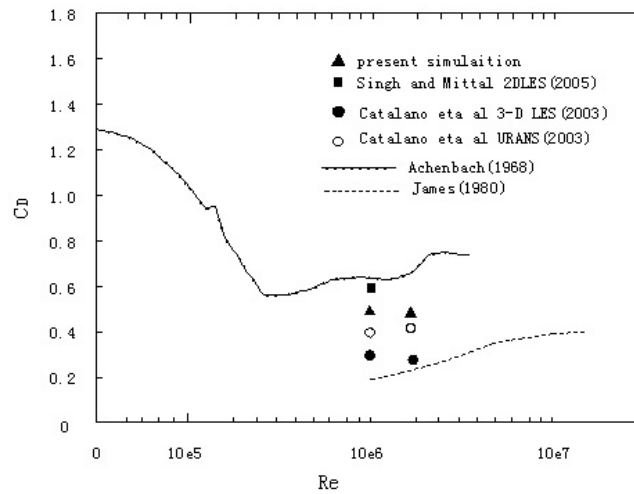


Fig. 6 Comparison of mean drag coefficients as a function of the Reynolds number

Table 1 comparison of mean drag coefficients at different Reynolds number

Re	Present method	Park <i>et al.</i>	Ye <i>et al.</i>
10	2.87	2.78	-----
20	2.06	2.01	2.03
40	1.59	1.51	1.52
80	1.42	1.35	1.37
300	1.21	1.37	1.38

### 5.2 Validation of fluid-structure interaction

To verify the accuracy of the simultaneous solution procedures for fluid-structure interaction, the 2D fluid-structure interaction benchmark problem in laminar flow described in Turek *et al.* (2006) was computed, in which FSI2 test denotes unsteady 2D fluid-structure corresponding to the final benchmark settings. Thus, FSI2 test was computed for the validation of the proposed procedure. This test is well-documented in the aforementioned reference, and thus it will only be described briefly. As can be seen from Fig. 7, the geometry consists of a horizontal channel of 0.41 m high, containing a rigid cylinder with radius of 0.05 m and center positioned 0.2 m above the bottom of the channel, i.e., center located at (0.2,0.2,) (from the lower left position of the computational domain), and an elastic bar behind the cylinder with length  $l = 0.35$  m and height  $h = 0.02$  m, with lower right position located at (0.6,0.19), whose left side is completely connected with the fixed cylinder. The control point A(t) is fixed in the middle of the elastic bar end with  $A(0) = (0.6, 0.2)$ . The mean inlet velocity for FSI2 test is 10m/s. Pressure contours in the vicinity of the structure at different time of the FSI2 test are shown in Fig. 7.

Fig. 8 shows displacements of node A in different directions. The results are compared to those in Turek *et al.* (2006). It can be observed that the results agree well with those from the aforementioned reference.

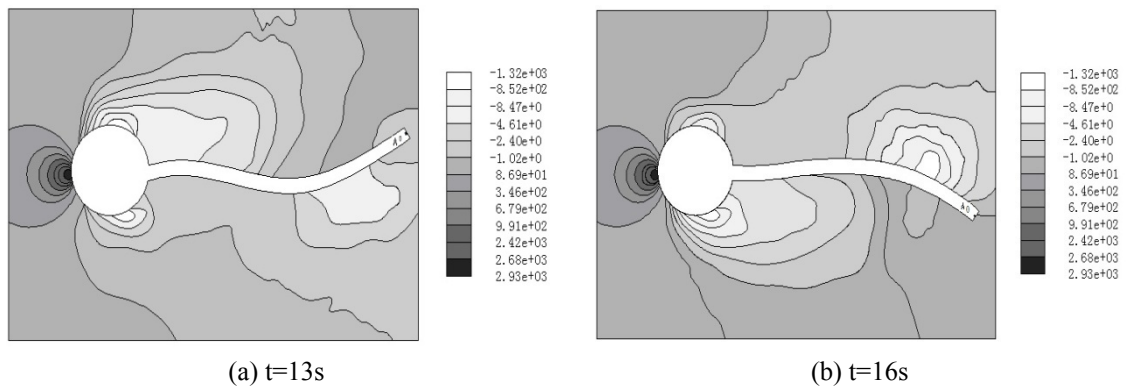


Fig. 7 Pressure contours at different times of the FSI2 test. (a) $t=13s$  and (b) $t=16s$

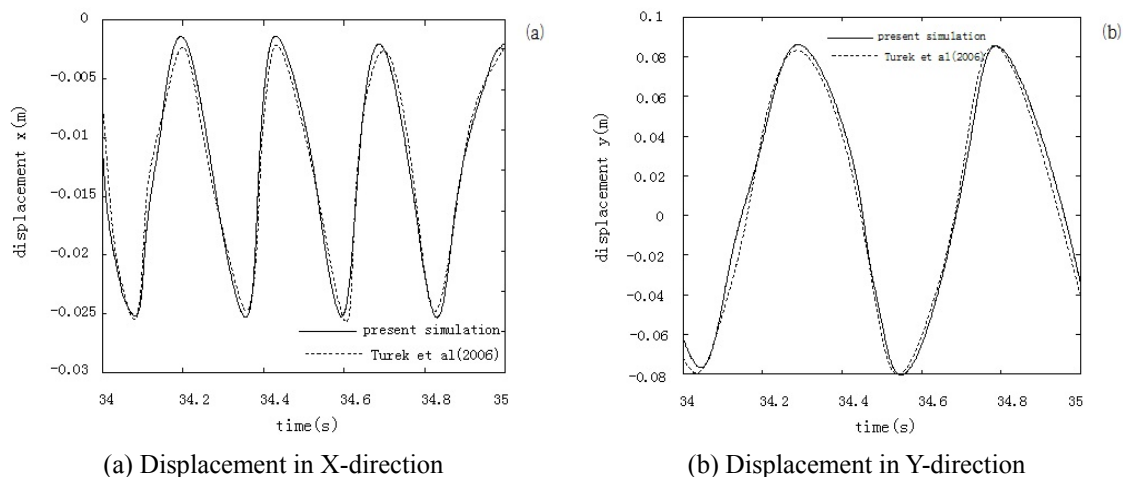


Fig. 8 Comparison of displacements of node A on elastic beam

## 6. Fluid-structure interaction of saddle membrane structures under wind actions

Fluid-structure interaction of a saddle membrane structure under wind actions is simulated and analyzed. The configuration of the structure is shown in Fig. 9. The computation conditions are as follows.

The structure span is 20 m and height is 5 m with rise-span ratio of  $f/L=1/8$ . The membrane thickness is 1mm, with density of  $1.25\text{kg/m}^2$ , tensile stiffness  $E_t=8.0\times 10^5\text{N/m}$ , shear stiffness  $G_t=1.2\times 10^4\text{N/m}$ , and Poisson's ratio  $\nu=0.3$ . The objective of this paper is to evaluate the performance of the proposed simultaneous solution procedures in computation of wind-membrane interaction, and the consideration of upwind turbulence effect will definitely make the computation more complicated. Thus, the effect of upwind turbulence is not taken into account; this would possibly affect the fluid velocity and relevant parameters such as mean pressure distributions, fluctuating pressures of the membrane, etc. as a result. More computation time would be required if upwind turbulence is included. However, the fundamental conclusions such as the effects of FSI on wind pressure distribution, membrane responses, and added mass and damping, etc. would not be affected. It should be noted that these first results without upwind turbulence provide experiences about the performance and accuracy of simultaneous solution in computation of wind-membrane interaction, and ideas on how to overcome the difficulties arising.

The first four vibration modes and corresponding frequencies are computed, as shown in Fig. 10. Terrain type C is simulated, according to the national building code of China,  $\alpha=0.22$  is chosen. The inlet wind profile obeys the power law, with a mean wind velocity of 10.32m/s.  $0^\circ$  wind azimuth is defined as along the diagonal connecting the two high points, while  $90^\circ$  wind azimuth is along the diagonal connecting the two low points, as shown in Fig. 11.

In addition, when calculating responses of the membrane, structural damping is considered in the initial stage to establish steady fluid field. While during the main stage (when the fluid field reaches its real flow state, i.e. fully developed vortex shedding, and the membrane structure enters its real vibration state) of fluid-structure interaction, structural damping ratios of  $\xi=0$  (Michalski

and Kermel 2011) and  $\xi=0.02$  are computed, respectively.

The computation domain was set as  $240\text{ m}\times 180\text{ m}\times 40\text{ m}$ , with the membrane structure center set at  $80\text{ m}$  from the entrance. The fluid domain was discretized with about  $264,000$  elements, while  $6,000$  elements were used for the membrane structure. The meshing of the membrane structure is shown in Fig. 12. A slip boundary condition was applied to the upper wall of the fluid domain while a no-slip boundary condition was applied to the lower wall and the interface.

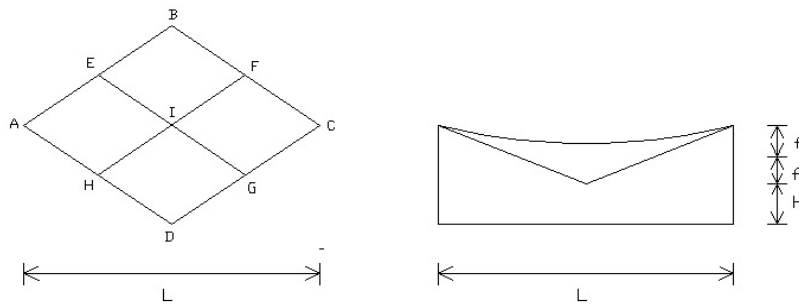


Fig. 9 Geometry of saddle membrane structure

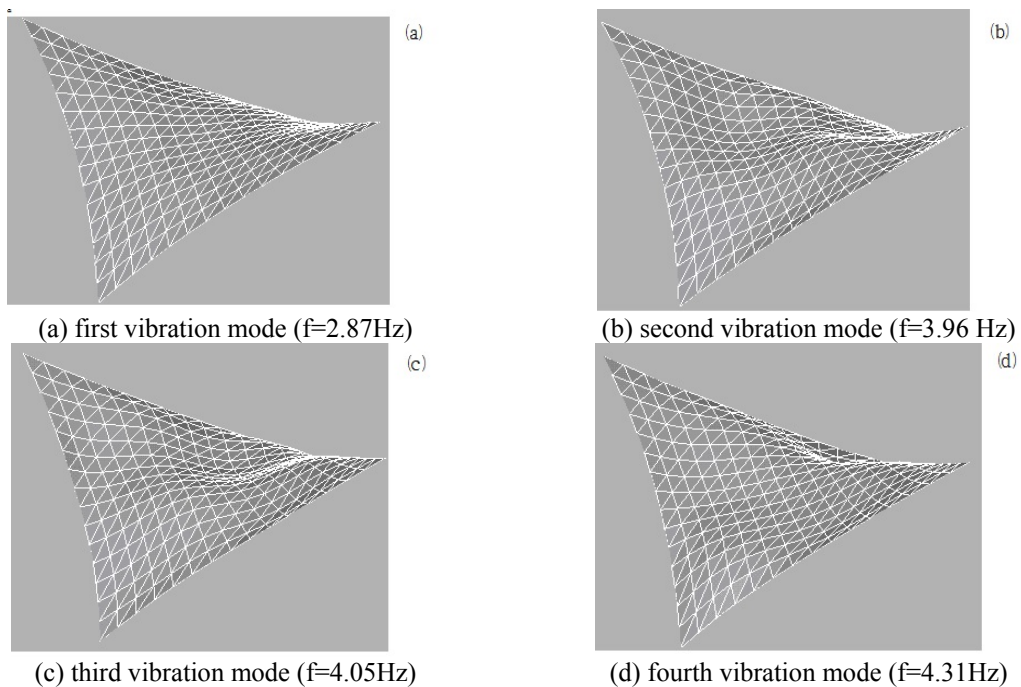


Fig.10 First four vibration modes and corresponding frequencies

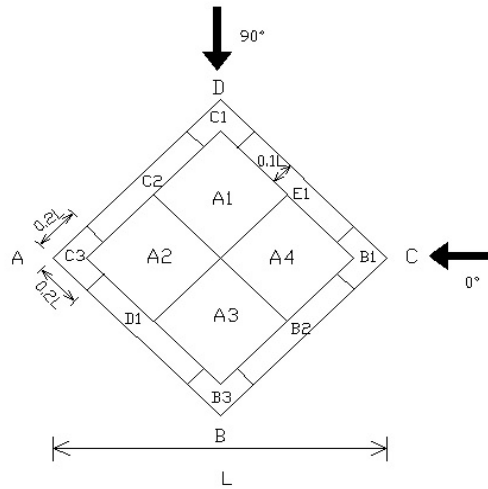


Fig. 11 Dividing of saddle membrane structure

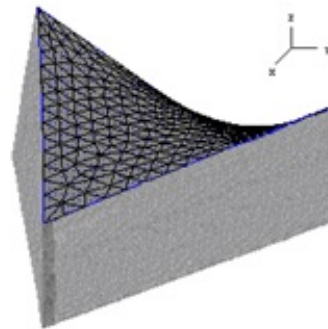


Fig. 12 Meshing of saddle membrane structure

At first, wind pressure coefficients of the membrane structures were computed. The time step was chosen as 0.01 s and 25 total iterations were used. The computation was considered to be converged when the norms of the computed element stress and the exact stress are less than  $10^{-4}$ . Given the inlet velocity of the entire fluid domain, the simulation starts. After experiencing unsteady pressure peaks of several time steps, the velocity field starts to converge. The computing time length is set to be  $t=200s$ .

According to the characteristics of shape and wind pressure distribution of the saddle membrane structure, the roof was divided into 12 areas (Uematsu *et al.* 1999), that is, corner areas (B1 , B3 , C1 , C3), lateral areas (B2 , C2 , D1 , E1), and middle areas (A1 , A2 , A3 , A4), as shown in Fig. 11.

Computation was performed both including, and not including, fluid-structure interaction. Two cases were used without fluid-structure interaction. That is, (a) the membrane structure does not vibrate, (b) the membrane structure vibrates, but fluid-structure interaction is not considered. Thus, there are three cases for computation: (a) the membrane structure does not vibrate, (b) the

membrane structure vibrates but fluid-structure interaction is not considered, (c) The membrane structure vibrates and fluid-structure interaction is considered.

The mean values of net wind pressure coefficients and R.M.S values of fluctuating pressure coefficients for each area of the structure for case (a) described above at 0° and 90° wind azimuths are listed in Table 2.

Analyzing data from Table 2, it can be concluded that,

(1) Wind suction dominates on the membrane structure surface. Larger wind suction is located near windward edge, with a large gradient, which is caused by strong separation of flow at the windward leading edge of the structure.

(2) Different pressure distributions are obviously observed for different divided areas at different wind azimuths. At 0° wind azimuth, negative wind pressures appear in some areas. All the areas are subjected to wind suction at 90° wind azimuth, with high negative wind pressure areas. The maximum negative wind pressure appears at 90° wind azimuth, which indicates the most severe separation of flow at the leading edge of the structure.

Wind pressure time histories of the membrane center I were computed for case (a) including FSI and, case (b) for not including FSI at different wind azimuths when considering structural damping, respectively (in the following part, the cases of not including FSI are all referred to case (b) described above), as shown in Fig. 13.

As can be seen from Fig. 13, wind pressure coefficients are different for cases of including FSI and not including FSI, but are all negative. The reason for the difference between the two conditions is that structural deformation caused by FSI alters the surrounding flow distribution, and alters wind pressure distribution on the structure as a result.

Table 2 Net wind pressure coefficient at typical wind azimuths for case (a)

area	wind azimuth	0°		90°	
		Mean wind pressure coefficient ( mean )	Fluctuating wind pressure coefficient(R.M.S)	Mean wind pressure coefficient ( mean )	Fluctuating wind pressure coefficient(R.M.S)
A1		-0.52	0.13	-1.29	0.17
A2		-0.34	0.06	-1.07	0.08
A3		-0.22	0.04	-1.33	0.07
A4		-0.54	0.07	-1.20	0.06
B1		-1.56	0.21	-1.26	0.03
B2		-1.35	0.15	-1.30	0.03
B3		-0.86	0.03	-1.09	0.02
C1		-0.76	0.02	-1.78	0.23
C2		-0.15	0.02	-1.53	0.16
C3		-0.13	0.01	-1.28	0.09
D1		0.18	0.04	-1.36	0.04
E1		-1.28	0.14	-1.37	0.12

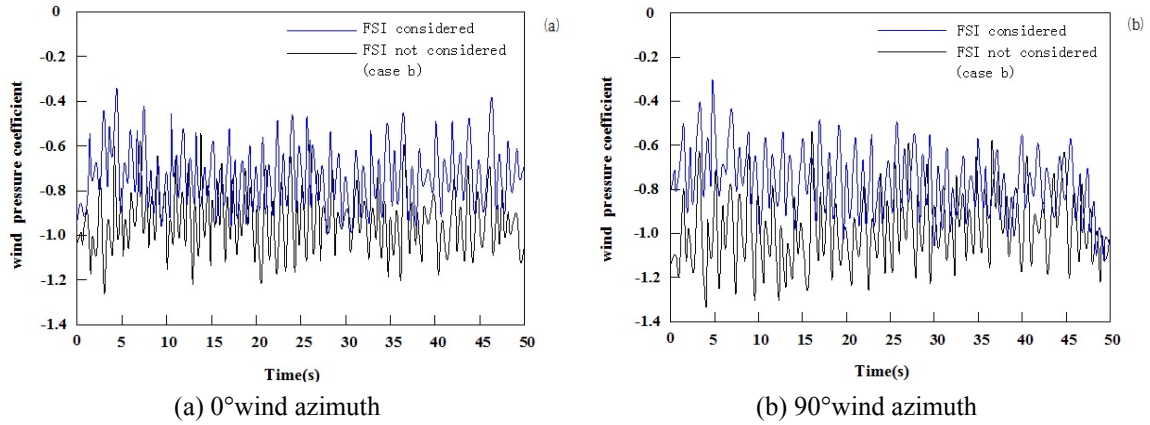


Fig. 13 Wind pressure time histories of middle point I at different wind azimuth

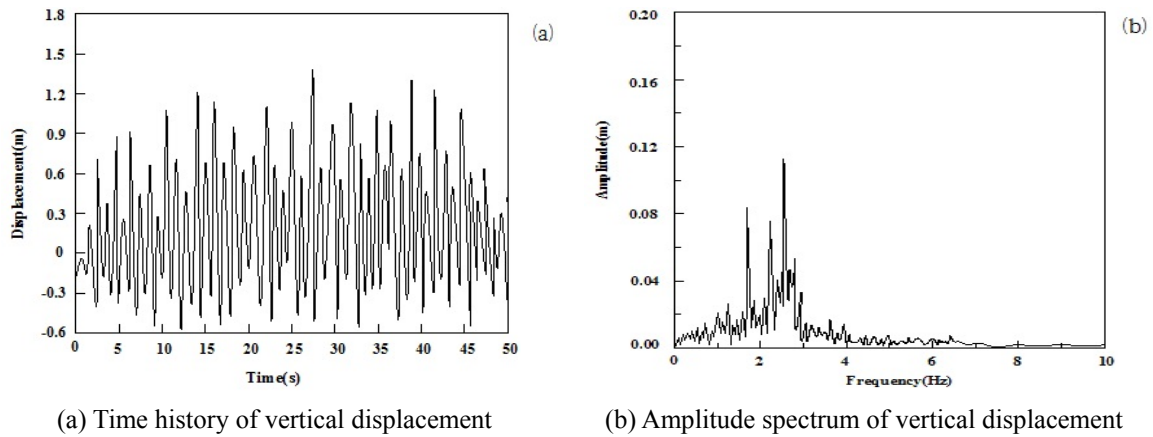


Fig. 14 Vertical displacement time histories and amplitude spectra of membrane center without considering FSI (structural damping considered)

Vertical displacement time histories and amplitude spectra of the membrane center I in case of concluding FSI and not including FSI at  $0^\circ$  wind azimuth when considering structural damping are shown in Figs. 14 and 15, respectively. Fig. 16 shows vertical displacement time histories and amplitude spectra of middle point I including FSI when structural damping is not taken into account.

Analyzing the results of Figs. 14 to 16, it can be concluded that,

(1) As Figs. 14 and 15 show, wind-induced responses including FSI are less than those not including FSI, which indicates that FSI inhibits the wind-induced responses, and causes energy dissipation. According to the study from Minami *et al.* (1996), on the premise of aero-elastic stability, the aerodynamic damping value is generally positive. Consideration of fluid-structure interaction amounts to taking aerodynamic damping into account. Hence, the wind-induced responses for including FSI are less than those not including FSI.

(2) As shown in Figs. 15 and 16, the displacement amplitude spectra including FSI (whether structural damping is considered or not), it can be seen that the vibration of the membrane

structure is a process with wide frequencies and low amplitudes. The structural responses are mostly distributed among the low frequency bands, and the energy for the first natural frequency is also small, which illustrates the structure responses are mainly background responses. From the displacement amplitude spectra not including FSI, it can be seen that displacement amplitudes mainly distribute among frequency bands from 1.6Hz up to 3Hz, including the membrane first natural frequency of 2.87Hz, and the vibration energy is larger than that of including FSI. However, the displacement responses are still background responses for the case of not including FSI.

(3) Through comparison of Figs. 15 and 16, it can be concluded that structural vibration is affected merely by aerodynamic damping when structural damping is not considered, and the displacements without considering the structural damping are much larger than those considering the structural damping.

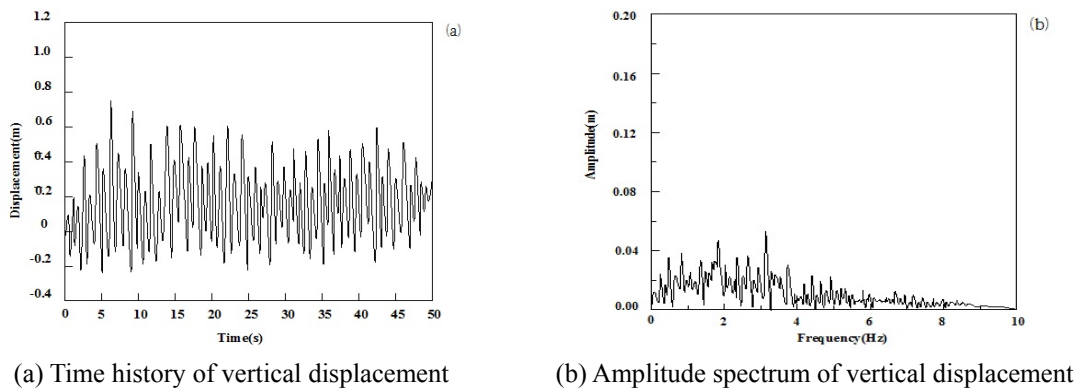


Fig. 15 Vertical displacement time histories and amplitude spectra of membrane center considering FSI (structural damping considered)

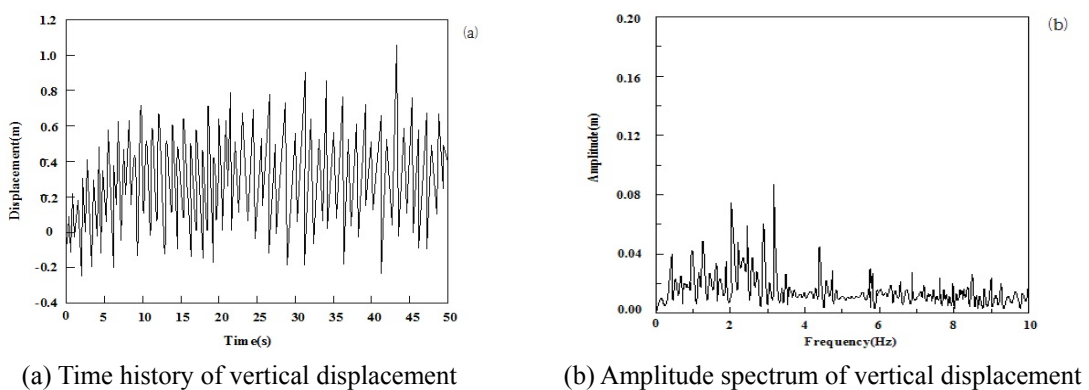


Fig. 16 Vertical displacement time histories and amplitude spectra of membrane center considering FSI (without considering structural damping)

During the computation, it was found that including FSI, it took 98 hours on high-performance personal computers to computing structural responses for the first 50 s under wind actions, whereas 56 hours were needed for not including FSI. That is, 43% extra computation time were needed in the case of including FSI. In addition, to demonstrate efficiency of the proposed method in this work, the commercial software ANSYS-CFX was adopted for comparison. It took about 80 hours to compute the first 50s time histories, saving about 18% computation time compared with the proposed method here. It is because that for the simultaneous solution procedures, computation of global matrix is needed.

In addition, to illustrate the effects of aerodynamic damping on the membrane vibration under wind actions, the random decrement technique (Marukawa *et al.* 1996) was applied to identify the modal parameters of the structure responses to obtain curves of attenuation, from which total damping ratio  $\xi_a$  was identified. The aerodynamic damping  $\xi_a = \xi - \xi_s$ , where  $\xi_s$  is the structural damping of the model. The variation of aerodynamic damping for the first three vibration modes with increase of wind velocities at  $0^\circ$  and  $90^\circ$  wind azimuths is shown in Fig. 17. As can be seen from Fig. 17, (1) for all wind azimuths, aerodynamic damping tends to increase as wind velocity increases. (2) for different wind azimuths, aerodynamic damping corresponding to the first vibration mode is the largest, with the value among 0.05 to 0.08 for  $0^\circ$  wind azimuth, and 0.08 to 0.1 for  $90^\circ$  wind azimuth. The largest aerodynamic damping for  $90^\circ$  wind azimuth reaches about 0.1, five times the structural damping (structural damping  $\xi_s = 0.02$ ), which illustrates great effects of aerodynamic damping on the membrane responses under wind actions. Thus, aerodynamic damping must be considered in the membrane vibration under wind actions. The aerodynamic damping corresponding to the second and third vibration mode decreases with the increase of vibration mode. (3) Aerodynamic damping at  $90^\circ$  wind azimuth is larger than that at  $0^\circ$  wind azimuth. (4) Comparisons are made for the aerodynamic damping corresponding to the first vibration mode obtained from references Sun (2007) and Zhang (2005). In Sun (2007) and Zhang (2005), the aerodynamic damping of similar saddle membrane structure to that used in the present work at different wind azimuths, wind velocities, and vibration modes were studied. The results from Sun (2007) are in dashed line in Fig. 19, and it can be seen that there is difference between the results here and those from studies of Sun (2007) at different wind azimuths, while the general variation tendency is the same. The reason may lie in the differences of the membrane structure in Sun (2007), such as different span ( $L = 28$  m), rise span ratio ( $f/L = 1/12$ ) and the resulting natural frequencies (first two natural frequencies were 2.26 Hz and 3.03 Hz, respectively). Furthermore, in reference Sun (2007), aerodynamic damping is obtained from analytical expressions derived by theories of aeroelasticity, resulting in the different aerodynamic damping. Zhang *et al.* (2005) employed wavelet transformations to calculate aerodynamic damping of saddle membrane structures, in which the first two natural frequencies were 15.19 Hz and 24.77 Hz. Aerodynamic damping at a wind velocity of 15 m/s was 0.075 at  $0^\circ$  wind azimuth, and 0.053 at  $90^\circ$  wind azimuth, less than that at  $0^\circ$  wind azimuth. However, for all other wind velocities in Zhang *et al.* (2005), aerodynamic damping at  $90^\circ$  wind azimuth were all larger than those at  $0^\circ$  wind azimuth, which is of the same variation law in the present work.

Meanwhile, added mass of the membrane structure at wind velocity of 12 m/s is studied. When structure vibrates in the air, it may induce some of its surrounding air to vibrate as well. Thus, the effective structural mass includes structure mass as well as added mass induced by the structure vibration. For membrane structures, the added mass may be of the same magnitude as the membrane mass or even larger. Thus, the effects of added mass on the dynamic characteristics of these lightweight structures can not be ignored.

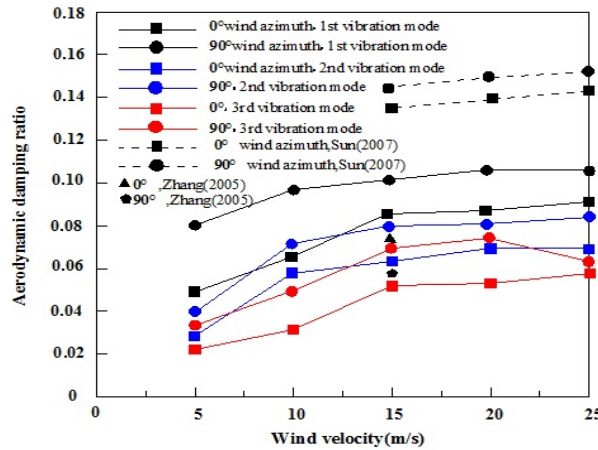


Fig. 17 Aerodynamic damping V.S. wind velocity

Sun (2007) employed theories of aeroelasticity to derive expressions of added mass of membrane structures, with the same parameters described above for aerodynamic damping. Mao (2004) derived the added air mass of open membrane structures, by thin airfoil theory, and discussed various factors affecting the value of the added air mass. According to Sun (2007), the added mass is mainly affected by the aerodynamic force on the structure surface and structural displacement. The aerodynamic force term in the added mass expressions is derived by theories of aeroelasticity. Based on the added mass and aerodynamic force expressions in Sun (2007), combined with the displacement calculated in the present work, the added mass variation with increase of vibration modes of open saddle membrane structure is calculated at different wind azimuths and rise-span ratio, as shown in Fig. 18.  $Z$  in the figure represents a non-dimensional added mass (Mao 2004) ( $Z=m_{a0}/\rho l$ ,  $m_{a0}$  is defined as added air mass on the unit membrane area, and  $\rho$  is the air density,  $l$  is the horizontal length along the membrane).

As can be seen from Fig. 18,

(1) Despite of the variation of wind azimuths or rise span ratio, added air mass of the membrane decreases as the number of vibration modes increases, with a large decreasing extent, that is, the lower vibration mode is, the greater added mass is. The added mass corresponding to the first natural vibration mode is the largest, with non-dimensional added mass among 0.54 to 0.63.

(2) The added mass at 90°wind azimuth is less than that at 0°wind azimuth. The non-dimensional added mass corresponding to the first five vibration modes varies from 0.53 to 0.60.

(3) The added mass decreases as the increase of rise-span ratio, with a large decreasing extent. It is because that with the increase of rise span ratio, the membrane structure rigidity increases as well, resulting in weakening of FSI between the membrane and the wind.

(4) According to the results for aerodynamic damping of open saddle membrane structures from Mao (2004), when  $H/l$  varied from 0 to 0.1 ( $H$  was maximum vibration amplitude of the membrane structure),  $Z$  varied from 0.6766 to 0.6871 accordingly, which is close to the results of 0.63 to 0.64 at 0°wind azimuth in this work.

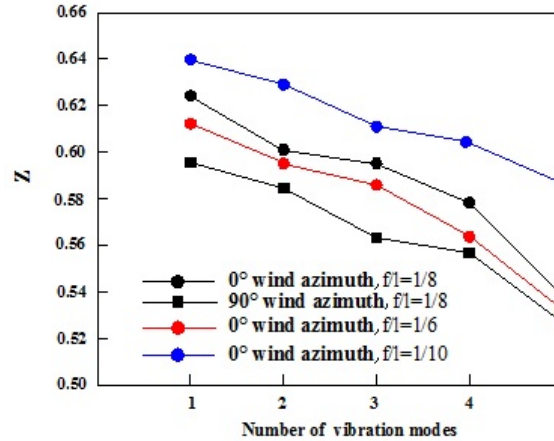


Fig. 18 Variation of non-dimensional added mass

## 7. Conclusions

This paper has studied the application of numerical simultaneous solution procedures to fluid-structure interaction of membrane structures under wind actions. The numerical methodologies for the simultaneous solution procedures are described. Special emphasis is placed on the coupling approach. Some preliminary explanations of the mechanism of FSI effects on membrane structures are given as follows:

(1) Wind suction dominates on the saddle membrane structure surface. Larger wind suction is located near the windward edge and with a large gradient, which is caused by strong separation of flow at the windward leading edge of the structure. Different pressure distributions are observed for different divided areas of saddle membrane structures at different wind azimuths.

(2) Responses under wind actions including FSI are less than those not including FSI, which indicates that FSI inhibits the structure responses under wind action, and causes energy dissipation.

(3) Vibration of the membrane structure under wind actions is a process with wide frequencies and low amplitudes when considering FSI. The structural responses are mostly distributed across low frequency bands. The displacement responses of the membrane structures are mainly background responses.

(4) The aerodynamic damping is a positive value, and increases with the increase of wind velocities. Moreover, the aerodynamic damping corresponding to the first vibration mode is the largest, much larger than the structural damping of the membrane.

(5) Added air mass of the membrane structure decreases as number of vibration modes increases. The added mass corresponding to the first natural vibration mode is the largest, with non-dimensional added mass among about 0.54 to 0.63. In addition, the added mass decreases as the increase of rise-span ratio of the structure.

(6) Considering the requirements for the upwind turbulence, it is obvious that further improvements are necessary to precisely define the wind loads. However, these first results provide experiences about the feasibility and accuracy of simultaneous solution in computation of wind-membrane interaction, and ideas on how to overcome the difficulties arising.

## Acknowledgments

The research described in this paper was financially supported by National Natural Science Foundation of China (Contract No. 51108345), opening foundation of State Key Laboratory for Disaster Reduction in Civil Engineering of China (Contract No. SLDRCE-MB-04), Opening research fund of Jiangsu key laboratory of engineering mechanics (Southeast University) and Foundation of Liaoning province education administration (Contract No. L2013134), which are gratefully acknowledged.

## References

- Achenbach, E. (1968), "Distribution of local pressure and skin friction around a circular cylinder in cross-flow up to  $Re=5 \times 10^6$ ", *J. Fluid Mech.*, **34**, 625-639.
- Bathe, K.J. and Ledezma, G.A. (2007), "Benchmark problems for incompressible fluid flows with structural interactions", *Comput. Struct.*, **85**(11-14), 628-644.
- Catalano, P., Wang, M., Iaccarino, G. and Moin, P. (2003), "Numerical simulation of the flow around a circular cylinder at high Reynolds numbers", *Int. J. Heat Fluid Fl.*, **24** (4), 463-469.
- Degroote, J., Bathe, K.J. and Vierendeels J. (2009), "Performance of a new partitioned procedure versus a monolithic procedure in fluid-structure interaction", *Comput. Struct.*, **87**(11-12), 793-801.
- Etienne, S. and Pelletier, D. (2004), "A monolithic formulation for steady-state fluid-structure interaction problems", *Proceedings of the 34th AIAA Fluid Dynamics Conference and Exhibition*, Portland, Oregon, U.S.A., 28 June - 01 July.
- Förster, C., Wall, W.A. and Ramm, E. (2005), "On the geometric conservation law in transient flow calculations on deforming domains", *Int. J. Numer. Meth. Fl.*, **50**(12), 1369-1379.
- Gil, A.J. (2006), "Structural analysis of prestressed Saint Venant-Kirchhoff hyperelastic membranes subjected to moderate strains", *Comput. Struct.*, **84**(15-16), 1012-1028.
- Glück, M., Breuer, M., Durst, F., Halfmann, A. and Rank, E (2003), "Computation of wind-induced vibrations of flexible shells and membranous structures", *J. Fluid. Struct.*, **17**(5), 739-765.
- Habchi, C., Russeil, S. and Bougeard, D. (2013), "Partitioned solver for strongly coupled fluid-structure interaction", *Comput. Fluids*, **71**, 306-319.
- Hachem, E., Feghali, S., Codina, R. and Coupez, T. (2013), "Anisotropic adaptive meshing and monolithic Variational Multiscale method for fluid-structure interaction", *Comput. Struct.*, **122**, 88-100.
- Heil, M. (2004), "An efficient solver for the fully coupled solution of large-displacement fluid-structure interaction problems", *Comput. Method. Appl. M.*, **193**(1-2), 1-23.
- Hoffman, J. and Jansson, N.A. (2011), *A Computational study of turbulent flow separation for a circular cylinder using skin friction boundary conditions*, Quality and reliability of large-eddy simulations II; ERCOFTAC series, Netherlands: Springer.
- Hübner, B., Walhorn, E. and Dinkler, D. (2004), "A monolithic approach to fluid-structure interaction using space-time finite elements", *Comput. Method. Appl. Mech. Engrg.*, **193**(23-26), 2087-2104.
- James, W.D., Paris, S.W. and Malcolm, G.N. (1980), "Study of viscous crossflow effects on circular cylinders at high Reynolds numbers", *AIAA J.*, **18**(9), 1066-1072.
- Li, C., Li, Q.S., Huang, S.H., and Xiao, Y.Q. (2010), "Large eddy simulation of wind loads on a long-span spatial lattice roof", *Wind Struct.*, **13**(1), 57-83.
- Li, H.N., Yi, T.H., Jing, Q.Y., Huo, L.S. and Wang, G.X. (2012), "Wind-induced vibration control of Dalian international trade mansion by tuned liquid dampers". *Math. Probl. Eng.*, **2012**(2012), 1-20.
- Lima, A.L.F., Silva, E., Silveira-Neto, A. and Damasceno, J.J.R (2003), "Numerical simulation of two-dimensional flows over a circular cylinder using the immersed boundary method", *J. Comput. Phys.*, **189**(2), 351-370.

- Mao, G.D., Sun, B.N. and Lou, W.J. (2004), "The added air mass for membrane structures", *Eng. Mech.*, **21**(1), 153-158.
- Marukawa, H., Katon, N., Fujii, K. and Tamura, Y. (1996), "Experimental evaluation of aerodynamic damping of tall buildings", *J. Wind Eng. Aerod.*, **59**(2-3), 177-190.
- Michalski, A., Haug, E., Bradatsch, J. and Bletzinger, K.U. (2009), "Virtual design methodology for lightweight structures – aerodynamic response of membrane structures", *Int. J. Space Struct.*, **24**(4), 211-221.
- Michalski, A., Kermel, P.D., Haug, E., Löhner, R., Wüchner, R. and Bletzinger, K.U. (2011), "Validation of the computational fluid-structure interaction simulation at real-scale tests of a flexible 29 m umbrella in natural wind flow", *J. Wind Eng. Aerod.*, **99**(4), 400-413.
- Minami, H., Okuda, Y. and Kawamura, S. (1996), "The critical condition for occurrence of fluttering of membrane suspended in uniform air flow", *J. Wind Eng.*, **1996**(66), 27-34.
- Park, J., Kwon, K. and Choi, H. (1998), "Numerical solutions of flow past a circular cylinder at Reynolds number up to 160", *J. Mech. Sci. Technol.*, **12**(6), 1200-1205.
- Revuz, J., Hargreaves, D.M. and Owen, J.S. (2012), "On the domain size for the steady-state CFD modelling of a tall building", *Wind Struct.*, **15**(3), 313-329.
- Richter, T. (2013), "A fully Eulerian formulation for fluid–structure-interaction problems", *J. Comput. Phys.*, **233**, 227-240.
- Stein, K., Tezduyar, T. and Benney, R. (2003), "Mesh moving techniques for fluid-structure interactions with large displacements", *J. Appl. Mech. - TASME*, **70**(1), 58-63.
- Singh, S.P. and Mittal, S. (2005), "Flow past a cylinder: shear layer instability and drag crisis", *Int. J. Numer. Meth. Fl.*, **47**(1), 75-98.
- Stein, K., Tezduyar, T. and Benney, R. (2003), "Mesh moving techniques for fluid-structure interactions with large displacements", *J. Appl. Mech. - TASME*, **70**(1), 58-63.
- Sun, X.Y. (2007), *Study on wind-structure interaction in wind-induced vibration of membrane structures*, Ph.D. Thesis, Harbin Institute of Technology, China.
- Turek, S. and Hron, J. (2006), *Proposal for numerical benchmarking of fluid-structure interaction between an elastic object and laminar incompressible flow*, Lecture Notes in Computational Science and Engineering .
- Uematsu, Y. and Isyumov, N. (1999), "Wind pressures acting on low-rise building", *J. Wind Eng. Ind. Aerod.*, **82**(1-3), 1-25.
- Yang, W., Quan, Y., Xinyang, J., Tamura, Y. and Gu, M. (2008), "On the influences of equilibrium atmosphere boundary layer and turbulence parameters in CWE", *J. Wind Eng. Ind. Aerod.*, **96**(10-11), 2080-2092.
- Wüchner, R., Kupzok, A. and Bletzinger, K. (2007), "A framework for stabilized partitioned analysis of thin membrane - wind interaction", *Int. J. Numer. Meth. Fl.*, **54**(6-8), 945-963.
- Ye, T., Mittal, R., Udaykumar, H.S. and Shyy, W. (1999), "An accurate Cartesian grid method for viscous incompressible flows with complex boundaries", *J. Comput. Phys.*, **156**(2), 209-240.
- Yang, Y., Gu, M., Chen, S. and Xinyang, J. (2009), "New inflow boundary conditions for modeling equilibrium atmosphere boundary layer in CWE", *J. Wind Eng. Ind. Aerod.*, **97**(2), 88-95.
- Zhang, L.Q., Li, H., Wu, Y. and Shen, S.Z. (2005), "Identification of wind vibration frequency and aerodynamic damping of cable-membrane structures base on wavelet transformation", *Proceedings of the 12th National Academic Conference on Wind Engineering*, China, October.
- Zienkiewicz, O.C. and Zhu, J.Z. (1992a), "The super convergent patch recovery and a posteriori error estimates, Part 1: the recovery technique", *Int. J. Numer. Meth. Eng.*, **33**(7), 1331-1364.
- Zienkiewicz, O.C. and Zhu, J.Z. (1992b), "The super convergent patch recovery and a posteriori error estimates, Part 2: error estimates and adaptivity", *Int. J. Numer. Meth. Eng.*, **33**(7), 1365-1382.